

## Breaks in lithology: Interpretation problems when handling 2D structures with a 1D approximation

Alan Yusen Ley-Cooper<sup>1</sup>, James Macnae<sup>2</sup>, and Andrea Viezzoli<sup>3</sup>

### ABSTRACT

Most airborne electromagnetic (AEM) data are processed using successive 1D approximations to produce stitched conductivity-depth sections. Because the current induced in the near surface by an AEM system preferentially circulates at some radial distance from a horizontal loop transmitter (sometimes called the footprint), the section plotted directly below a concentric transmitter-receiver system actually arises from currents induced in the vicinity rather than directly underneath. Detection of paleochannels as conduits for groundwater flow is a common geophysical exploration goal, where locally 2D approximations may be valid for an extinct riverbed or filled valley. Separate from effects of salinity, these paleochannels may be conductive if clay filled or resistive if sand filled and incised into a clay host. Because of the wide system footprint, using stitched 1D approximations or inversions may lead to misleading conductivity-depth images or sections. Near abrupt edges of an extensive conductive layer, the lateral falloff in AEM amplitudes tends to produce a drooping tail in a conductivity section, sometimes coupled with a

local peak where the AEM system is maximally coupled to currents constrained to flow near the conductor edge. Once the width of a conductive ribbon model is less than the system footprint, small amplitudes result, and the source is imaged too deeply in the stitched 1D section. On the other hand, a narrow resistive gap in a conductive layer is incorrectly imaged as a drooping region within the layered conductor; below, the image falsely contains a blocklike poor conductor extending to depth. Additionally, edge-effect responses often are imaged as deep conductors with an inverted horseshoe shape. Incorporating lateral constraints in 1D AEM inversion (LCI) software, designed to improve resolution of continuous layers, more accurately recovers the depth to extensive conductors. The LCI, however, as with any AEM modeling methodology based on 1D forward responses, has limitations in detecting and imaging in the presence of strong 3D lateral discontinuities of dimensions smaller than the annulus of resolution. The isotropic, horizontally slowly varying layered-earth assumption devalues and limits AEM's 3D detection capabilities. The need for smart, fast algorithms that account for 3D varying electrical properties remains.

### INTRODUCTION — AIRBORNE ELECTROMAGNETICS IN HYDROGEOLOGY

Some of the first quantitative applications of airborne electromagnetics (AEM) in mapping fresh ground- and saline waters and in subsurface geomorphological regolith delineation were put forward by Fitterman and Deszcz-Pan (1998) and Worrall et al. (1998, 1999). More recently, one-fourth of Denmark (> 10,000 km<sup>2</sup>) was mapped geophysically, targeting groundwater. AEM performed most of this mapping, and the method has repeatedly proven to scientifically support the management and understanding of groundwater (Danielsen et al., 2003). Baldridge et al. (2007) discuss applications of AEM in

New Mexico. A study of an AEM groundwater survey flown in Africa is presented by Sattel and Kgotlhang (2004). As part of a tender process, the Australian government has analyzed different AEM systems according to their suitability to detect predefined targets (Lawrie, 2009). The studies mentioned here are only a few of those available on AEM in hydrogeology applications.

Commonly, fast 1D conductivity and depth transforms from AEM point data collected along survey lines are stitched together to form approximate depth sections, sometimes known as conductivity-depth images. Various approximations and transforms have been presented in different modalities and variations, e.g., by Macnae et al. (1998), Christensen (2002), and Sattel (2005). The main advan-

Manuscript received by the Editor 5 October 2009; revised manuscript received 27 February 2010; published online 30 September 2010.

<sup>1</sup>Geoscience Australia, Canberra, Australia. E-mail: yusen.ley@ga.gov.au.

<sup>2</sup>School of Applied Sciences, RMIT University, Australia. E-mail: james.macnae@rmit.edu.au.

<sup>3</sup>University of Aarhus, Department of Earth Sciences, Aarhus, Denmark. E-mail: andrea.viezzoli@geo.au.dk.

© 2010 Society of Exploration Geophysicists. All rights reserved.

tage of these conductivity-depth images over apparent resistivities such as those defined for frequency-domain data (Siemon, 2001) is the estimated depth information they provide. In the AEM community, there has been some discussion as to when/whether these fast transforms should be replaced with constrained inversion processes. Brodie and Sambridge (2006) and recently Christensen et al. (2010) discuss the trade-off in time and computational restrictions that comes with inversion versus more accurate quantitative and better-resolved models of the subsurface geoelectrical structures. A key question is whether full, nonlinear 1D inversions are significantly better than the fast approximations when 2D or 3D structures are encountered.

Most of the available literature shows that interpretation of isotropic and slowly varying geoelectrical data is possible, using full inversion methods with constraints and fast conductivity transforms (Newman et al., 1987; Goldman et al., 1994; Hördt and Scholl, 2004; Auken et al., 2008; Viezzoli et al., 2008; Christensen et al., 2010). Because of the volume of data, AEM surveys usually are interpreted using stitched 1D models, although most interpreters are aware that geologic structures have a 3D spatial distribution. Despite successful 2D/3D EM modeling and inversion (Haber et al., 2004; Wilson et al., 2006), these multidimensional algorithms are very computationally demanding, which limits their applications on large data sets such as those acquired for AEM surveys, typically sampled every 3–10 m and resulting in millions of soundings per survey. Full 2D/3D inversion may take hours or even days of computer time per line-kilometer of data. Faster computers have cut costs and processing time, but data acquisition has ballooned for greater survey coverage, resulting in more data being collected in larger surveys.

This paper shows the correlation between resolution of penetration depth and sensitivity for AEM systems, and it highlights the risks of interpreting anisotropic horizontal variations, assuming a vertically varying layered solution using 1D forward responses or a fast conductivity transform. Macnae and Xiong (1998) note interpretation errors derived from stitching conductivity-depth sections where lateral variations (2D structures) are treated as a 1D problem. Farquharson et al. (2003) show the misleading effects of inverting frequency-domain data with susceptibility contaminated data. Airborne systems detect layer breaks and sharp edge boundaries before the system actually is above these layer discontinuities, but the signal and its associated 1D inversion are plotted directly below the AEM system (Wolffgram et al., 2003). Interpreting conductivities that are based on a 1D solution can generate deceptive depths and conductivity artifacts because the isotropic assumption no longer holds.

Any AEM response is defined by a geometric variation (system geometry) and a time or frequency response (West and Macnae, 1991). Here, we use examples of time- and frequency-domain AEM data. The EM response at the inductive limit (early step-delay times or high frequencies) is exactly equivalent and has the highest possible spatial resolution of any target in a resistive background (Macnae et al., 1998). The spatial implications as to lateral sensitivity in this paper should apply to time- and frequency-domain data for the same system geometry/altitude.

## DEPTH OF PENETRATION, ANNULUS OF RESOLUTION, AND FOOTPRINT

The depth of penetration  $D$  of an AEM system is not trivial to define. For a target in a resistive host, it depends on transmitter moment

and waveform, sensor, and electronic and turbulence system noise. A simple approximation is given by Macnae (2007), who predicts  $D$  as being on the order of several hundred meters for most AEM systems. As a result, many if not most hydrogeophysical targets easily fall within this depth of penetration. However, AEM systems have considerable lateral as well as depth sensitivity, and lateral sensitivity increases with increasing depth. There are several methods through which this lateral sensitivity can be defined. For the case of a thin-sheet conductor, typical of a thin saline layer in stratified geology, the contribution of induced currents to the received signal is easy to define through the receding-image (Grant and West, 1965) and adjoint-sensitivity methods (Ellis, 1999).

The thin-sheet adjoint sensitivity in its usual definition is the surface integral of the product of the electric fields of the transmitter and the virtual electric field of the receiver in the target (Ellis, 1999). If the vector product is used as defined in equation 10 of Ellis (1999), then the adjoint sensitivity measures the contribution, including sign of the actual induced currents in the uniform layer. If the scalar product is used, a scalar adjoint sensitivity is a measure of the maximum absolute sensitivity of the system to inhomogeneity in each area  $dA$ . For concentric loop systems, the scalar and vector adjoint sensitivities are identical. Because the actual electric field (current) in the thin sheet with step magnetic excitation can be estimated trivially at any delay time by Maxwell's receding-image solution (e.g., Macnae et al., 1991), the contribution of each area  $dA$  within the thin sheet to the overall sensitivity is trivial to compute. The induced currents in the sheet expand outward with delay time; however, the receiver (electric) sensitivity falls off as  $1/r^2$  and leads to a response arising from currents close to the receiver.

For a typical helicopter time-domain electromagnetic system (TEM) at a height of 50 m above the thin conductor, Figure 1 shows plots of the relative contributions of the induced currents at the inductive limit (the early time-step response) and at the limiting response at late delay times. The maximum contribution arises from an annular zone concentric with the TEM system.

With a horizontal loop transmitter of radius  $r$  flying at height  $h$ , the maximum currents initially induced in any layered conductor at depth  $d$  are centered on a circle of radius  $R$  at vertical offset  $(h + d)$  below the transmitter halo. We call the diffuse, doughnut-shaped ring of current around this maximum induced current (see Figure 1, top row) the initial *annulus of resolution* and quantify it with radius  $R$  (Figure 2). A first-order approximation at the inductive limit is that  $R \approx h + d + r$ , or that the maximum initial current flow in a superficial conductive layer has an approximate radius equal to the sum of transmitter height and loop radius. More detailed analyses by Beamish (2003) and Reid et al. (2006) define footprints of EM systems, which, alas, vary with several factors and are not fixed in size or shape. Our annulus of resolution is very similar in principle but conceptually is a function that can change with circumstances (unlike footprints, which to us sound as if they should be of fixed shape and size).

The term *annulus* also implies the lack of current flow directly below the transmitter. After excitation, induced currents invariably expand outward and, if possible, downward in extended conductors; so the annulus of resolution will expand with delay time or for layers at greater depths. If the receiver is concentric with the transmitter, the EM system has an inherent annulus of resolution diameter of  $2(h + d + r)$  or greater. If the receiver is at a different altitude from the transmitter, reciprocity and heuristic arguments suggest that  $h$  in the above equation should be approximately the geometric mean height

of the transmitter-receiver pair. Fixed-wing AEM systems with 120-m-altitude transmitters and 90-m-high receivers would have an initial annulus of resolution two to three times the size of a helicopter system with a 25-m-diameter loop at an altitude of 30 m.

For fixed-wing geometries, the adjoint sensitivity for a vertical component receiver has a more complex shape (Beamish, 2003), which approximates an annulus for the  $z$ -component at the inductive limit. This sensitivity can be computed easily using adjoint fields and is, of course, receiver-component dependent (Figure 3). The inline  $x$ -component receiver has a more compact sensitivity function than the  $z$ -component. Figure 4 plots the sensitivities as a function of delay time along a central profile directly beneath the airborne system. Although the concentric-loop EM systems have an annular-sensitivity function where contributions are positive, the annular-current system beneath the fixed-wing transmitter  $z$ -component leads to sensitivities of either sign.

Because the response of a thin sheet of conductance  $S$  is given by the field of an image of the source at a depth of  $z = a + vt$  where  $a$  is the transmitter altitude,  $v$  is the receding velocity given by  $\mu_0 S/2$ , where in turn  $\mu_0$  is the magnetic permeability of free space. Defining a dimensionless depth as  $d = z/z_0$ , where  $z_0$  is the image depth at time zero, we can define a dimensionless time as identical to the dimensionless depth and give it the symbol  $d$ . Image depth is related linearly to time, so the EM response at dimensionless time  $d$  is also independent of thin-sheet conductance. When the depth of the receding image is double its starting value, we have  $d = 1$ . At this dimensional time, the concentric-loop AEM response amplitude will have dropped by about a factor of eight, assuming an inverse cube falloff in amplitude with distance.

## METHODS

We look at data from three different AEM systems: the fixed-wing TEMPEST system (Lane et al., 2000), a concentric-loop (Sattel, 2009) RepTEM system, and a six-frequency helicopter system. Commercially available helicopter-borne concentric loop systems include AeroTEM, RepTEM, SkyTEM, and VTEM. The systems differ in precise details of the transmitter waveform, base frequency, dipole moment, receiver-noise levels, and sampling. However, with similar geometries and waveforms, our conclusions regarding spatial resolution can be applied to any of these systems.

Separated transmitter-receiver AEM systems show more variation in geometry than the concentric-loop systems; HeliGEOTEM has a vertically offset receiver, and the fixed-wing systems such as TEMPEST, GeoTEM, and MEGATEM have receivers behind and below the aircraft-mounted transmitter. These systems have less lateral resolution than concentric-loop systems.

Frequency-domain systems vary in the number of frequencies, separation between coils, and actual transmitting frequencies used. Although more flexible than time-domain systems on the desired configuration, each transmitter-receiver pair is an individual instrument that requires calibration and drift monitoring.

Heterogenous material and heavy weathering of existing rocks is to be expected in many parts of Australia; in some cases, this cover can be several hundred meters thick. In parts of the regolith below the cover, paleochannels once may have been incised into the landscape, causing breaks in pre-existing layers and creating lateral variations (Worrall et al., 1998). AEM often is applied to help map such targets. Paleochannel structures can have high-resistivity contrasts

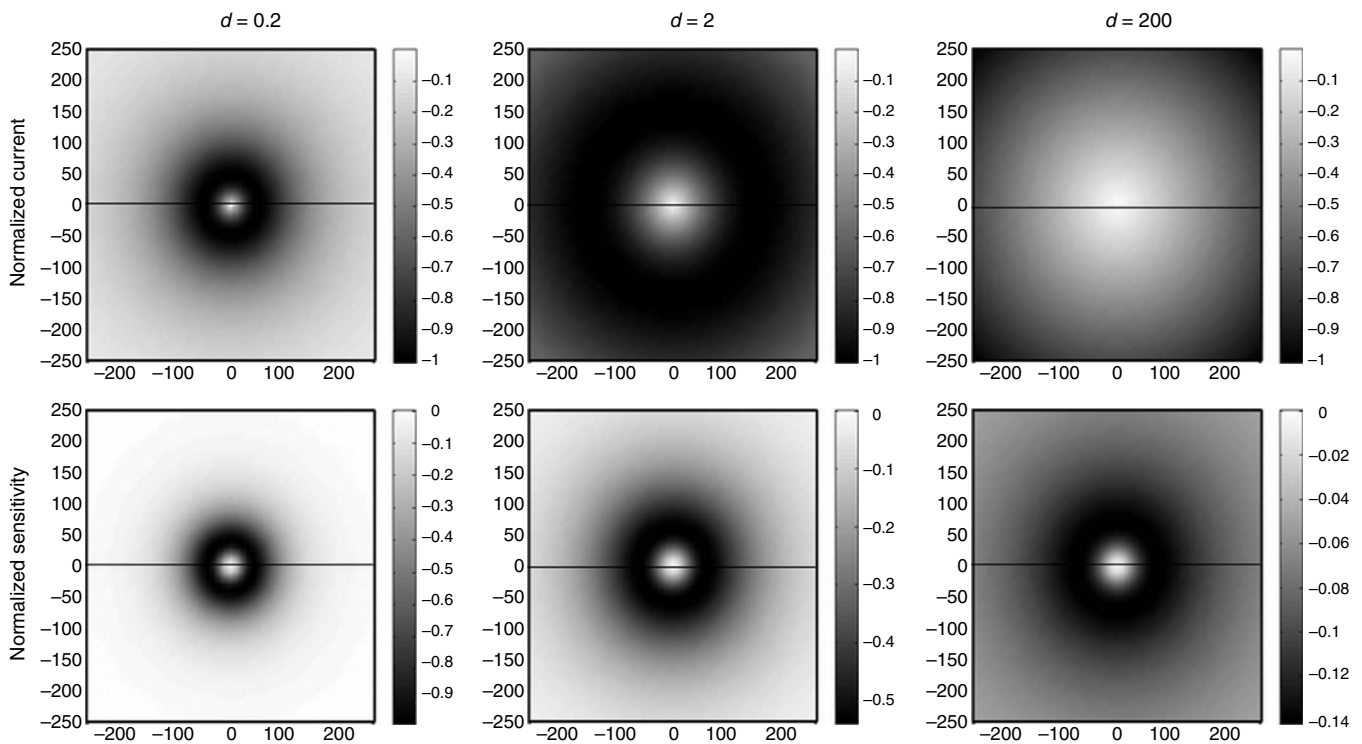


Figure 1. (Top row) Current density maps (normalized to peak value) at normalized delay times  $d$ , showing the outward expansion of induced currents. (Bottom row) Contribution of induced currents to observed AEM step response, showing the limited expansion of the annulus of resolution with delay time.

with their surroundings, we present cases where the 1D assumption on AEM data cannot reliably resolve lithology boundaries and depths.

The use of 2D/3D inversions to deal with sharp boundaries and edge effects has been suggested (Haber et al., 2004); but even with the rapid increase in computing speed, execution times are unrealistically long for extensive AEM data sets. We have used several modeling codes in this analysis: Arjuna Air, EMFlow, and Aarhus Workbench laterally constrained inversion (LCI).

Forward-modeling data for paleochannel environments were calculated using Arjuna Air (Wilson et al., 2006), which models the airborne system as a magnetic dipole transmitter with one magnetic dipole receiver. Solutions for the frequency domain are obtained by transformation into a mixed spatial-Fourier domain, whereas time-domain responses are obtained from six-frequency responses and a Hankel transform convolved with the transmitter-system waveform.

EMFlow (Macnae et al., 1998) is an industry-standard, fast method for transforming AEM data to a conductivity-depth image (CDI).

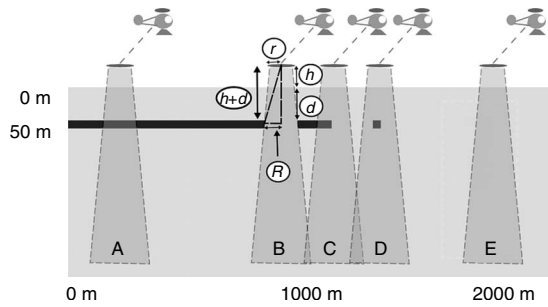


Figure 2. Different positions of AEM receivers. An EM sensor of radius  $r$  detects and registers the target before the instrument's transmitter is fully above the conductive layer, at radius  $R$ , imaging a dipping conductor (an edge effect) with a vertical exaggeration of 10:1. The black discontinuous conductor at 50 m depth is used as a model for disrupted layering.

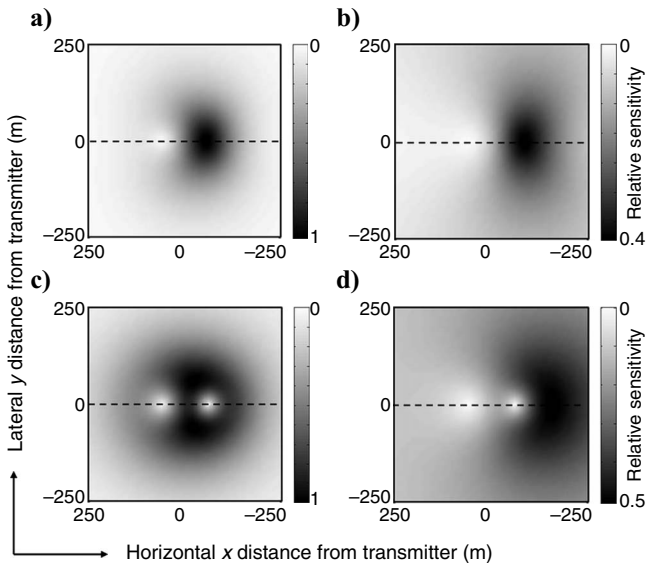


Figure 3. Scalar adjoint sensitivity map to show relative maximum contribution of currents induced in a thin sheet to a fixed-wing AEM receiver measuring (a, b) the vertical  $z$ -component and (c, d) the in-line or  $x$ -component, with (c, d) as at late delay times.

It first deconvolves the data to the time-constant domain and then uses the analytic receding-image solution of Maxwell to derive independent CDI values for each transient decay. The results are stitched together to form maps and sections.

The Aarhus Workbench LCI (Auken et al., 2005) is a full, nonlinear, least-squares damped inversion with lateral constraints. The forward responses are exact layered-earth responses, based on Ward and Hohmann (1988), and contain the description of the full system transfer function. The lateral constraints included in the inversion limit the variability of model parameters of adjacent soundings to the

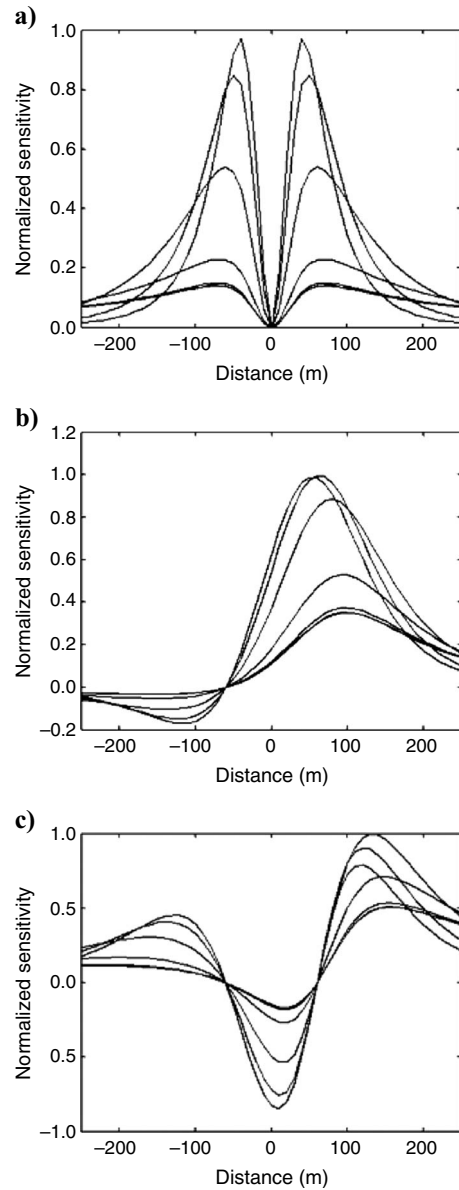


Figure 4. Thin-sheet vector adjoint sensitivity as a function of system and delay time, plotted in the flight direction as a function of the horizontal distance of induced currents from the transmitter. These profiles correspond in location to the horizontal lines in Figures 1 and 3. Curves have dimensionless time units of 0.06, 0.2, 0.6, 2, 6, 20, and 60. The largest amplitudes are at the inductive limit, and the smallest are at late delay times. These plots show that thin-sheet currents contribute positively and negatively to the overall fixed-wing system response. (a) Concentric loop height of 50 m. (b) Fixed-wing  $x$ . (c) Fixed-wing  $z$ .

degree of geoelectrical variability expected in the area. In this way, the output models balance the information contained within every sounding with the information from the constraints, reducing the parameter variance. Further prior information from, say, conductivity logs also can be added to the inversion and can migrate to neighboring soundings via the constraints. In the spatially constrained inversion (Viezzoli et al., 2008), not applied in this manuscript, the constraints are set not just along flight lines but also across them, exploiting fully the spatial geologic coherence.

## RESULTS

Paleochannel mapping is important in several scenarios. These may be related to mineral exploration (e.g., placer diamond or gold deposits, uranium) or water resource mapping. In cases such as in northeastern Victoria, Australia, paleochannels contain conductive clays and magnetic minerals. Figure 5 shows the combination of a TEMPEST survey, processed to produce an AEM conductivity map derived from stitched CDIs, superimposed with magnetic shading. The result is a detailed image of a paleodrainage system. Dendritic features can be detected migrating to the center and northeast on the map. Imaged conductivity that increases down these paleochannels can be interpreted as higher salinity concentrations in the environment. Figure 6 presents a typical conductivity-depth section over what has been interpreted as four adjacent paleochannels, linked to the location on the map. All of the conductive features mapped by these TEMPEST data are considerably wider than the annulus of resolution, which has a radius of approximately 150 m at shallow depths.

The CDI sections derived from 1D approximation seem spatially coherent despite the wide sensitivity and asymmetry of the fixed-wing AEM system. Paleochannels are not, however, always as wide or as conductive as the ones mapped in this example. West of Broken Hill in New South Wales, Australia, paleochannels cutting through older saline clay layers show up as relatively resistive features in map form. The fastest methods of AEM modeling over extensive areas involve stitching together 1D solutions to make 2D and eventually 3D models. Figure 7 is an example of two lines of RepTEM AEM data, each about 3 km long, transformed to CDI sections with the EMFlow program. In this area west of Broken Hill, a moderately conductive layer, about 80 m thick, lies beneath a near-surface,

mostly resistive layer. Shallow, intermittent conductors are present within the resistive layer.

Evident within the conductive cover in both sections shown in Figure 7 is a thin, very conductive layer at a depth of about 50 m. This layer underlies transported cover and is interpreted from nearby drilling to map the location at depth of saline, clay-rich materials from a former lake bed. The conductivity-depth section of line 1090, with slight undulations in the saline conductive layer, has one obvious gap marked as A. This response is spatially correlated with similar responses on adjacent lines, with the corresponding location on line 1070 marked by dashed lines. There are several additional discontinuities on line 1070, such as an apparent bulge/thinning of the saline layer at B and saline-layer depth undulations with near-surface expressions at C. A key interpretation question to be answered is whether the apparent gaps in the thin, conductive layer indicate complete absence of the clays caused by a paleochannel that was incised through the buried clays in later years or whether resistive gaps are depositional variations, thinning the layer. A simple approach might be to use 2D or 3D inversion methods to address this, but current 2D

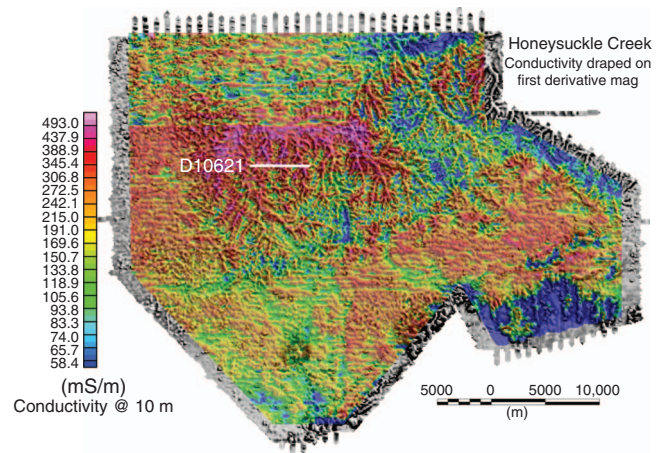


Figure 5. The Honeysuckle Creek survey in Australia was flown with a TEMPEST fixed-wing towed-bird time-domain system. This image shows a conductivity map at a depth of 10 m draped over first-derivative magnetics. Note the dendritic paleochannel mapping to the center and northeast of the survey.

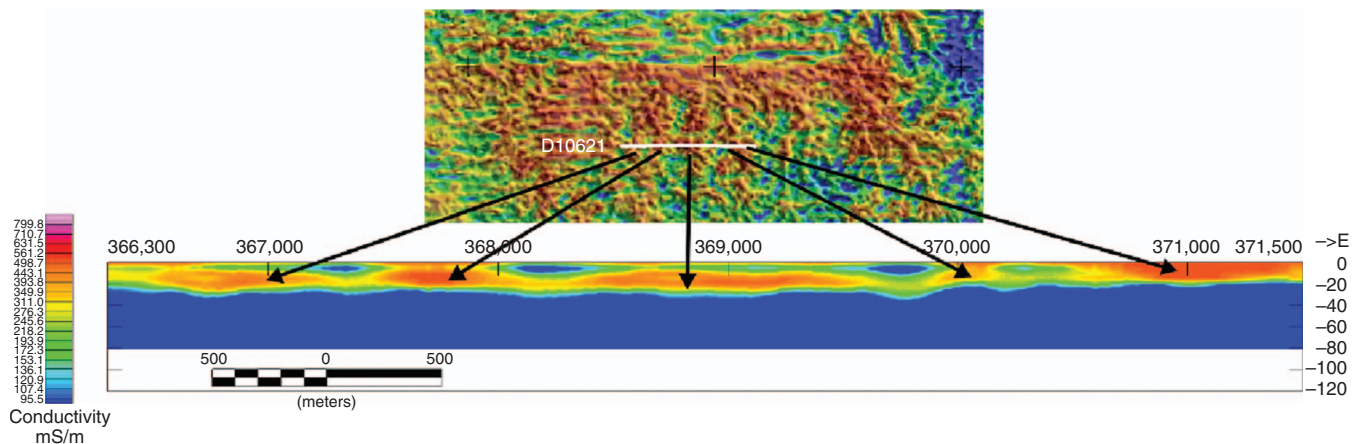


Figure 6. EMFlow conductivity-depth section (CDI) of TEMPEST data from the Honeysuckle Creek survey in Figure 5. Close-up shows high-conductivity structures coincident with the existing paleochannels, also mapped by the magnetics.

and 3D inversion for AEM data is very slow and quite dependent on choice of initial model and lateral/smoothing constraints.

We therefore decided to test the horizontal resolution and accuracy of stitched 1D sections of some 2D cases representative of the two hydrogeologic problems described above. We start with the analysis of a 133-m-wide gap in a conductive layer. We modeled the AEM response with the Arjuna Air program (Wilson et al., 2006) for a generic helicopter time-domain system with a 25-m-diameter transmitter and a dipolar concentric diameter receiver, flying at a height of 35 m. Such a system can be expected to have an annulus of resolution, or footprint, of 100–200 m (Figure 1), within which annulus most (say, 90%) of the observed response is generated. EM systems that can detect targets to depths of many hundreds of meters also detect conductors at lateral distances of this order.

Forward responses calculated from the synthetic models (Figure 8) were converted to conductivity-depth sections (Figure 9), with

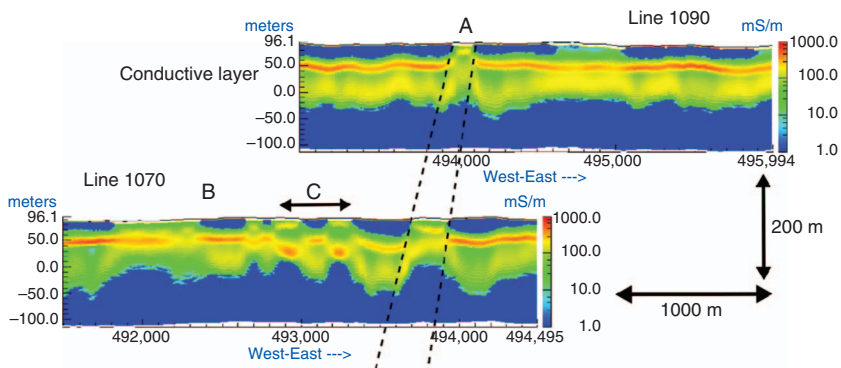


Figure 7. EMFlow conductivity-depth sections from a Reptem AEM system flown in the Broken Hill area show several discontinuities and gaps (marked as A) on lines 1090 and 1070, an apparent bulge/thinning of the saline layer at B (approximately 50 m deep), and saline-layer depth undulations with near-surface expressions at position C.

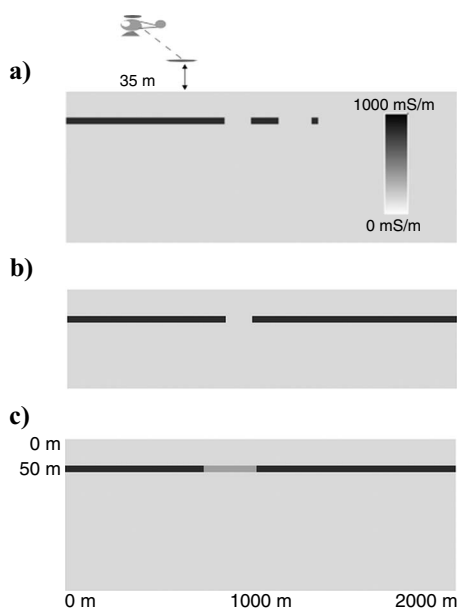


Figure 8. Synthetic forward models calculated using Arjuna Air, for a six-frequency towed-bird system, a coincident loop, and a fixed-wing platform with towed receiver. (a, b) A conductive 1000-mS/m broken layer in a resistive 1-mS/m host (models 1 and 2). (c) An intermediate filling conductor of 333.33 mS/m shown in model 3.

EMFlow. The extended layer (in synthetic model 1) is correctly imaged close to its true vertical extent from 51 to 64 m deep, with reasonably accurate estimates of its true conductivity of 1000 mS/m. Because of smoothing inherent in the EM induction process, the images show a moderately conductive halo above and below the thin, very conductive layer. Because of edge effects, rather than an abrupt termination of the conductor at the left and right boundaries (true location, in white), the resistive gap appears on the stitched image as a blocky, moderate conductor about 50 mS/m extending to depth, with a drooping edge and deep horseshoe-shaped response of about 200-mS/m anomalies at depth. The drooping edge response is the effect of the AEM system “seeing” the layer ahead or behind as it flies down the line but plots directly below the system. The deep, upside-down horseshoe responses come from edge effects where current induced in the layer concentrates near its edge and causes a small high in the EM response.

This synthetic gap response is very different from the interpreted paleochannel response at A in Figure 7. The response at A has no obvious drooping tail; rather, the conductor at depth trends under the layer rather than away from it, as seen in Figure 9b. The conclusion would need to be that the incised paleochannel at A in Figure 7 is not an electrical resistor but has an internal conductivity structure. Alternatively, the response at depth may droop away from the near-surface ribbon conductor above the main layer.

Figure 9a shows a slightly more complex 2D model we tested. It consists of a discontinuous conductor (conceptually representing a discontinuous saline clay layer) at a depth of 50 m. The layer extends off the profile to the left, and two separate segments of 133 and 33 m width, with gaps of 133 and 167 m between them, respectively.

We call these conductor segments (from left to right) the layer, the wide ribbon conductor, and the narrow ribbon conductor.

Quite clearly, the 1000-mS/m left uniform layer in Figure 8a has been properly identified in Figure 9 (with some limitations in vertical resolution). The wide ribbon has been detected at the proper place but is imaged as a weaker conductor located on the deep side; a simplistic visual interpretation would probably underestimate its true width.

Because of its small amplitude, the narrow ribbon appears as an upside-down horseshoe of about 200-mS/m response in the CDI at a depth of about 250 m rather than as a horizontal ribbon at the true 50-m depth. In the gaps between the layer and the ribbons, we again see a blocklike artifact of about 50-mS/m conductivity.

The final synthetic data (Figure 9c), for a concentric-loop AEM system, consists of a single thin layer of 1000-mS/m conductivity; the central 267-m portion of the profile has a lower conductivity of 333.33 mS/m. In this case, the CDI image is visually correct, in that the layered conductor is imaged at the right depth and with the right conductivity-thickness product. No drooping-tail edge effects are seen, but there is a 50-mS/m block artifact underneath the less conductive zone.

Because TEMPEST is a fixed-wing, towed-bird AEM system, we would expect that edge effects and resulting artifacts in a CDI would be quite different from the concentric-loop system we modeled earlier. The TEMPEST AEM system measures two components, along line  $x$  and vertical  $z$ , which in EMFlow are processed separately.

Then the conductivity-depth image can be derived from each of the  $x$ - and  $z$ -components or from both data components. Separate responses from each component are shown in Figure 10b and c. Differences between the CDIs derived from the  $x$ - and  $z$ -component data are an indication of departure from lateral homogeneity; the  $x$ -component is more prone to detect conductive horizontal discontinuities (Figure 10b). We should note that a 3-s (roughly 30-m) cosine stacking filter has not been applied to the modeling to exactly simulate actual TEMPEST data (as described in Sattel and Reid, 2006).

In Figure 11, the conductivity image produced from synthetic TEMPEST data detects the wide and the narrow ribbons; however the ribbons are at an apparent depth much greater than the true depth of 50 m from the synthetic model. Generally, the CDI section appears less well resolved than the CDIs from the concentric-loop systems. This is to be expected because of the greater (120-m) flight height of a towed-bird system with fewer recorded time-delay channels affecting vertical resolution.

We now can compare results (Figure 11) from the TEMPEST CDIs of the synthetic models in Figure 8 with the three thin-layer cases shown in Figure 9 using a concentric AEM system. In Figure 11c, the relatively resistive center of the 2D layer is not nearly as well resolved as with the concentric AEM system. This is the effect of the much wider annulus of resolution of a fixed-wing system at higher altitude. If we compare this synthetic response with the TEMPEST field data (Figure 5), it is reasonable to interpret that the whole near-surface layer is conductive, with the paleochannels more conductive than their surroundings. In Figure 6, the inductive features (paleo-

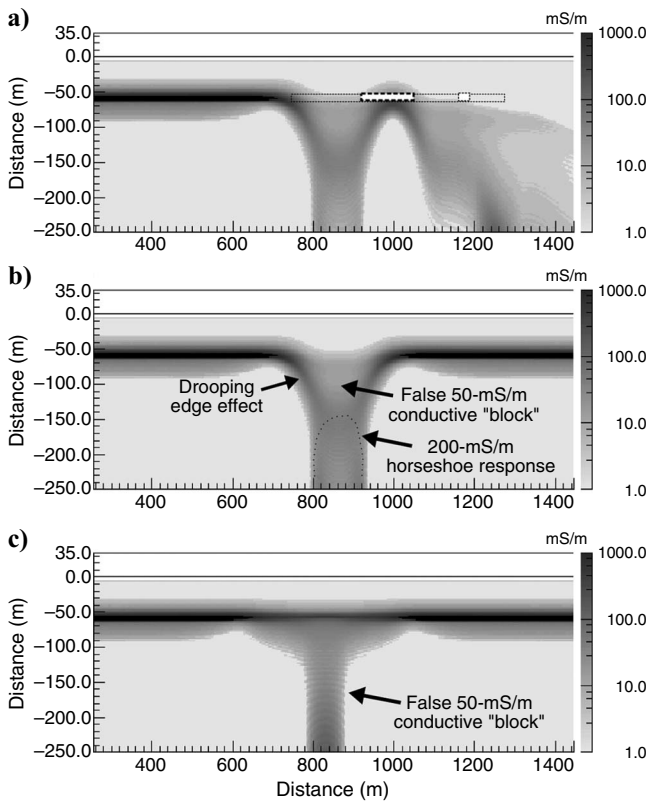


Figure 9. Conductivity-depth images calculated using EMFlow on synthetic concentric loop forward models calculated with Arjuna Air shown in Figure 8 for synthetic models (a) 1, (b) 2, and (c) 3.

ochannels) appear to have gently sloping rather than steep sides (in contrast to the incised structure of Figure 7).

Inversions can and should give more precise results over a 1D earth than fast conductivity transforms. However, we could not find

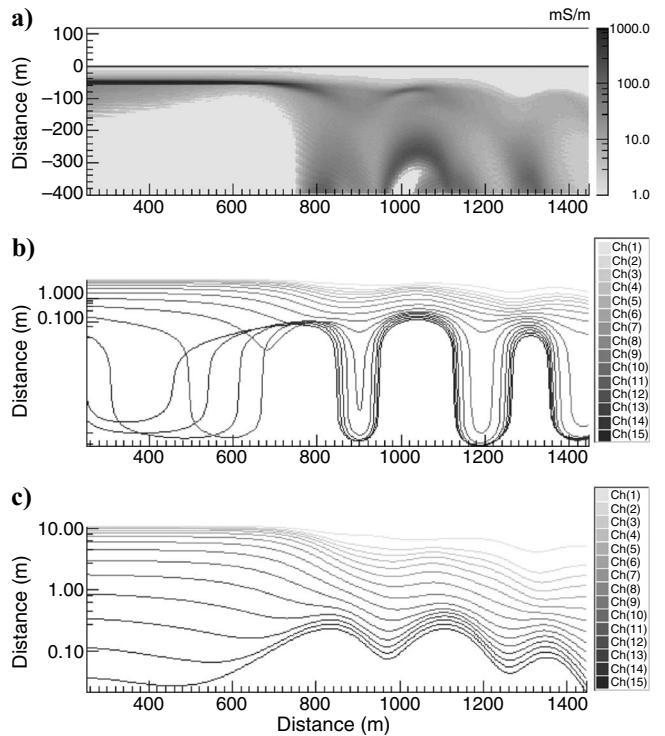


Figure 10. (a) Conductivity-depth image calculated using EMFlow on synthetic forward-modeled data from Arjuna Air model in Figure 8a, derived from both (b)  $x$ - and (c)  $z$ -components of TEMPEST data.

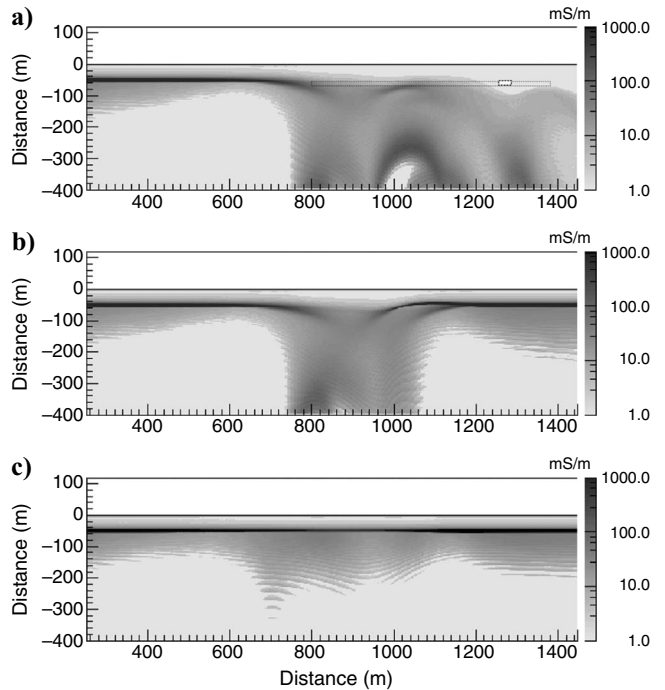


Figure 11. Conductivity-depth images calculated using EMFlow on synthetic (TEMPEST configuration) forward-modeled data calculated with Arjuna Air, for models (a) 1, (b) 2, and (c) 3 from Figure 8.

convincing evidence in the literature that stitching together a section made of independent or constrained 1D full inversions should have fewer artifacts than stitching together fast approximate transforms. Therefore, we tried to objectively analyze the limitations of laterally constrained inversions and fast transforms in the presence of horizontal inhomogeneities. To do so, we processed an identical six-frequency system forward model using a fast conductivity transform and a full laterally constrained inversion. Conductivity and depth results are shown in Figures 12 and 13, respectively.

Aarhus University in Denmark has commercialized a layered-earth inversion package called Aarhus Workbench (Viezzoli et al., 2008), optimized for use with AEM systems. We inverted our synthetic Arjuna Air frequency-domain forward-modeled data through Workbench. Several inversions with varying numbers of layers, depths, and lateral constraints were produced.

Figure 13 shows the LCI results of inversions of forward data corresponding to Figure 8a, with a smooth (19-layer) and blocky (5-layer) model. For the smooth case, the model space is discretized using 19 layers with layer thicknesses increasing with depth. The inversion only solves for layer resistivities. In the blocky case, the model space is discretized using five layers, and the inversion solves for layer resistivities and thicknesses. Both inversions were started from a homogeneous half-space of 10 ohm-m, so no prior information was input. The smooth and blocky models are consistent to produce similar results. As expected, the fewer-layers model (Figure 13b) recovers the absolute resistivity and thicknesses of the different layers better. Because this model has discontinuities in a simple layered environment, we focus on the fewer-layer results. The depth, thick-

ness, and resistivity of the extended-layer conductor on the left is well resolved. The wide-ribbon conductor is imaged as thicker and more resistive than its true values, and its depth is well resolved. The narrow-ribbon conductor produces a conductivity anomaly much deeper than its real location. The resistive gap between the left layer and the middle wide-ribbon conductor has about the right lateral size, but its resistivity value is underestimated (about 25 mS/m).

To establish some of the differences between the LCI and the CDIs, we focus on Figures 12a and 13b, the fewer-layers model. The results show how the LCI recovered the depth and extension of the extended layer and the wide-ribbon conductors satisfactorily. The break between them is visible, yet their resistivity is underestimated. The resistivity underneath the left extended conductive layer is overestimated; this is from lack of sensitivity of the specifically modeled frequency-domain system below that conductive layer. In Figure 12a, the depths to top and bottom of the left extended conductive layer are overestimated by about 10 m, whereas in the wide-ribbon depths are overestimated by more. The conductivity for both ribbons also is overestimated. The LCI and CDIs fail to recover the narrow ribbon, flagged by the high residual shown by the red curve superimposed on the models in Figure 13 (read against right axis, values greater than three are considered to be poor data fits). Regarding the resistive gap between left and center conductors, the LCI shows a

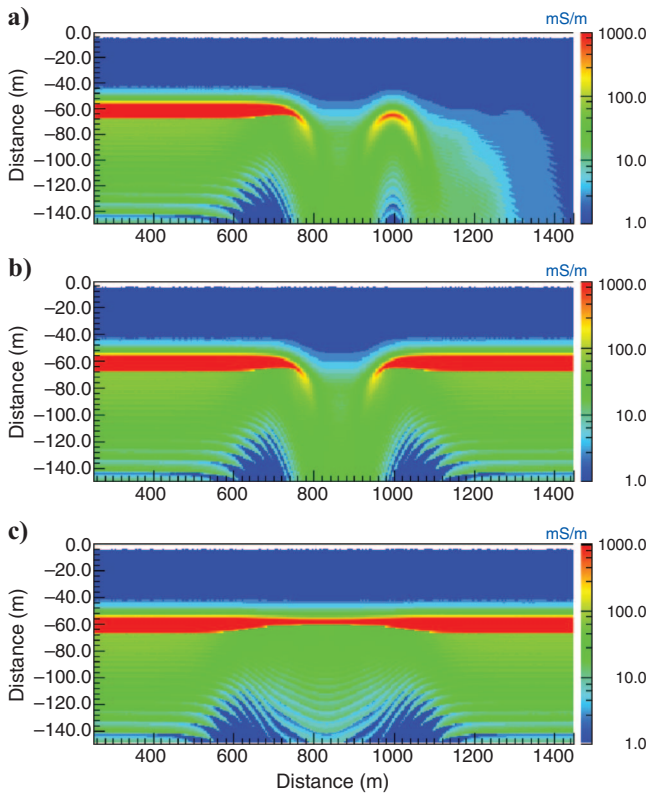


Figure 12. CDI of HEM system (six frequencies from 400 Hz to 130 kHz) from forward-modeled data calculated with Arjuna Air shown in Figure 8 for models (a) 1, (b) 2, and (c) 3.

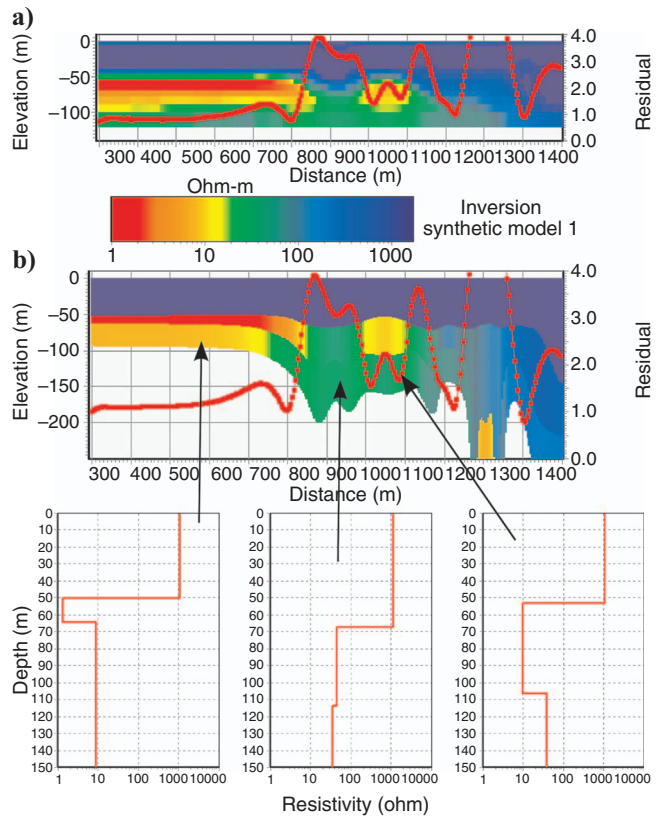


Figure 13. Inversion showing (a) smooth multi- (19-) layer and (b) fewer- (5-) layer inverted models for three different (critical) points flagged in Figure 8a. From left to right, (1) all layers are continuous, (2) the conductive layer is disrupted, and (3) the layer width is equal to the annulus of resolution. Inversion resolves the wide conductive ribbon's depth but at the expense of a large residual (red line superimposed on the models and read from the right axis). The narrow-ribbon conductor cannot be resolved and appears as a deep shadow in the section.

width of about 140 m, very close to the true one. The EMFlow results show the apparent gap to be quite wider, close to 200 m. Both image a false conductive block below the resistive gap.

Results show the LCI, just as EMFlow's CDIs and any other inversion based on exact or approximate 1D forward response, cannot fit the data at the edges of the conductors, where pronounced 2D effects are present. The lateral constraints in the LCI to a degree limit the vertical distortions of the models; however, very tight constrained inversions may incorrectly predict a thinning continuous layer to lateral distances away from its true source.

Overall, the two methodologies clearly produce results of similar lateral character. As expected, though, the LCI quantifies how well each model decay (taken in isolation) matches each individual data decay, at times indicating that a 1D decay cannot fit the data locally. The 1D approximate solutions such as EMFlow also produce such an error of fit; the LCI produces a model parameter sensitivity analysis and better recovers absolute values of resistivity, depth and thickness of extensive conductors, and lateral extent and resistivity value of the resistive gap between them.

## CONCLUSIONS

Regardless of the accuracy of the inversion algorithms, inversion is not an automated procedure. The results depend on correct parameterization and often on a good starting model. In particular, stitched 1D inversions of 2D/3D structures with sharp conductivity boundaries must be queried, even though the surroundings may be well modeled.

In electrically conductive environments, including weathered or sedimentary cover or where shallow saline water is present, any extensive subhorizontal conductor arising from saline water or clays will be detected by AEM. Such extensive structures are well imaged by approximate transforms and full nonlinear 1D inversions. Incised paleochannel structures or subvertical geologic boundaries within such environments may lead to lateral discontinuities in these more extensive conductive layers. When 2D/3D effects of these discontinuities are present, 1D CDI approximations and inversions may incorrectly predict a weaker conductor at depth within a resistive hole in the layer. Towed-bird systems will also produce edge effects and artifacts when processed with a 1D layered-earth assumption, but their different geometric responses in  $x$ - and  $z$ -components allow for easy detection of misleading 1D interpretations. Despite the fixed-wing systems' clear advantage to discern, having to fly at much higher altitude will impinge on their resolvability in the near surface because of their much wider annulus of resolution. In general, lateral constraints, as applied in the LCI, help produce models with lower degrees of vertical and lateral distortion if discontinuities are smaller than the annulus of resolution.

Within a conductive layer where conductivity changes with facies or geometric thickness, 1D approximations and LCI inversions can resolve the model well. Full inversions take more CPU time, and a high error of fit between a 1D model and data indicates lateral inhomogeneity in inversion and CDI approximate methods. As expected, few-layer LCI also recovers the absolute values of the geoelectrical layers better than smooth-model inversions. In the presence of conductivity anomalies of widths comparable to the annulus of resolution, 2D data modeling is needed to avoid misinterpretations of the subsurface, and methodologies to speed up existing inversion methods are very desirable for processing AEM data. This lateral limiting

width is on the order of 100 m for HEM systems and 250 m for fixed-wing systems.

## ACKNOWLEDGMENTS

The authors thank the Department of Primary Industries, Victoria, for letting us show data from the Honeysuckle Creek region, Callabonna Uranium Ltd. for letting us show parts of their Broken Hill HEM data, and the reviewers for their constructive comments.

## REFERENCES

- Auken, E., A. V. Christiansen, B. H. Jacobsen, N. Foged, and K. I. Sørensen, 2005, Piecewise 1D laterally constrained inversion of resistivity data: *Geophysical Prospecting*, **53**, 497–506.
- Auken, E., A. V. Christiansen, L. H. Jacobsen, and K. I. Sørensen, 2008, A resolution study of buried valleys using laterally constrained inversion of TEM data: *Journal of Applied Geophysics*, **65**, 10–20.
- Baldrige, W. S., G. L. Cole, B. A. Robinson, and G. R. Jiracek, 2007, Application of time-domain airborne electromagnetic induction to hydrogeologic investigations on the Pajarito Plateau, New Mexico, USA: *Geophysics*, **72**, no. 2, B31–B45.
- Beamish, D., 2003, Airborne EM footprints: *Geophysical Prospecting*, **51**, 49–60.
- Brodie, R., and M. Sambridge, 2006, A holistic approach to inversion of frequency-domain airborne EM data: *Geophysics*, **71**, no. 6, G301–G312.
- Christensen, N. B., 2002, A generic 1-D imaging method for transient electromagnetic data: *Geophysics*, **67**, 438–447.
- Christensen, N. B., A. Fitzpatrick, and T. Munday, 2010, Fast approximate 1D inversion of frequency domain electromagnetic data: *Near Surface Geophysics*, **8**, 1–15.
- Danielsen, J. E., E. Auken, F. Jørgensen, V. Søndergaard, and K. I. Sørensen, 2003, The application of the transient electromagnetic method in hydrogeophysical surveys: *Journal of Applied Geophysics*, **53**, 181–198.
- Ellis, R. G., 1999, Joint 3-D electromagnetic inversion, *in* M. Oristaglio, and B. Spies eds., *Three-dimensional electromagnetics, Part 3: Inversion*: SEG, 179–192.
- Farquharson, C. G., D. W. Oldenburg, and P. S. Routh, 2003, Simultaneous 1D inversion of loop-loop electromagnetic data for magnetic susceptibility and electrical conductivity: *Geophysics*, **68**, 1857–1869.
- Fitterman, D. V., and M. Deszcz-Pan, 1998, Helicopter EM mapping of salt-water intrusion in Everglades National Park, Florida: *Exploration Geophysics*, **29**, 240–243.
- Goldman, M., L. Tabarovsky, and M. Rabinovich, 1994, On the influence of 3-D structures in the interpretation of transient electromagnetic sounding data: *Geophysics*, **59**, 889–901.
- Grant, F. S., and G. F. West, 1965, *Interpretation theory in applied geophysics*: McGraw-Hill Book Company.
- Haber, E., U. M. Ascher, and D. W. Oldenburg, 2004, Inversion of 3D electromagnetic data in frequency and time domain using an inexact all-at-once approach: *Geophysics*, **69**, 1216–1228.
- Hördt, A., and C. Scholl, 2004, The effect of local distortions on time-domain electromagnetic measurements: *Geophysics*, **69**, 87–96.
- Lane, R., A. Green, C. Golding, M. Owers, P. Pik, C. Plunkett, D. Sattel, and B. Thorn, 2000, An example of 3D conductivity mapping using the TEM-PEST airborne electromagnetic system: *Exploration Geophysics*, **31**, 162–172.
- Lawrie, K. C., 2009, Broken Hill managed aquifer recharge project, [http://www.ga.gov.au/image\\_cache/GA15003.pdf](http://www.ga.gov.au/image_cache/GA15003.pdf), accessed 23 June 2010.
- Macnae, J., 2007, Developments in broadband airborne electromagnetics in the past decade: *Proceedings of the 5th International Conference on Mineral Exploration*.
- Macnae, J., A. King, N. Stoltz, A. Osmakoff, and A. Blaha, 1998, Fast AEM data processing and inversion: *Exploration Geophysics*, **29**, 163–169.
- Macnae, J. C., R. Smith, B. D. Polzer, Y. Lamontagne, and P. S. Klinkert, 1991, Conductivity-depth imaging of airborne electromagnetic step-response data: *Geophysics*, **56**, 102–114.
- Macnae, J., and Z. Xiong, 1998, Block modelling as a check on the interpretation of stitched CDI sections from AEM data: *Exploration Geophysics*, **29**, 191–194.
- Newman, G. A., W. L. Anderson, and G. W. Hohmann, 1987, Interpretation of transient electromagnetic soundings over three-dimensional structures for the central-loop configuration: *Geophysical Journal of the Royal Astronomical Society*, **89**, 889–914.
- Reid, J. E., A. Pfaffling, and J. Vrbancich, 2006, Airborne electromagnetic footprints in 1D earths: *Geophysics*, **71**, no. 2, G63–G72.
- Sattel, D., 2005, Inverting airborne electromagnetic (AEM) data with Zo-

- hdy's method: *Geophysics*, **70**, no. 4, G77–G85.
- , 2009, An overview of helicopter time-domain EM systems: Australian SEG, Extended Abstracts, doi: 10.1071/ASEG2009ab049.
- Sattel, D., and L. Kgotlhang, 2004, Groundwater exploration with AEM in the Boteti area, Botswana: *Exploration Geophysics*, **35**, 147–156.
- Sattel, D., and J. Reid, 2006, Modelling of airborne EM anomalies with magnetic and electric dipoles buried in a layered earth: *Exploration Geophysics*, **37**, 254–260.
- Siemon, B., 2001, Improved and new resistivity-depth profiles for helicopter electromagnetic data: *Journal of Applied Geophysics*, **46**, 65–76.
- Viezzoli, A., A. V. Christiansen, E. Auken, and K. Sørensen, 2008, Quasi-3D modeling of airborne TEM data by spatially constrained inversion: *Geophysics*, **73**, no. 3, F105–F113.
- Ward, S., and G. Hohmann, 1988, Electromagnetic methods in applied geophysics: SEG, 131–312.
- West, G. F., and J. C. Macnae, 1991, Physics of the electromagnetic induction exploration method, *in* M. N. Nabighian, ed., *Electromagnetic methods in applied geophysics*, vol. 2: Application: SEG, 5–45.
- Wilson, G. A., A. P. Raiche, and F. Sugeng, 2006, 2.5D inversion of airborne electromagnetic data: *Exploration Geophysics*, **37**, 363–371.
- Wolfgram, P., D. Sattel, and N. B. Christensen, 2003, Approximate 2D inversion of AEM data: *Exploration Geophysics*, **34**, 29–33.
- Worrall, L., T. Munday, and A. Green, 1998, Beyond bump finding — Airborne electromagnetics for mineral exploration in regolith dominated terrains: *Exploration Geophysics*, **29**, 199–203.
- , 1999, Airborne electromagnetics — Providing new perspectives on geomorphic process and landscape development in regolith-dominated terrains: *Physics and Chemistry of the Earth, Part A: Solid Earth and Geodesy*, **24**, 855–860.